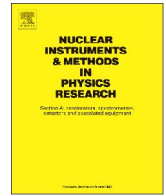




Contents lists available at ScienceDirect

# Nuclear Instruments and Methods in Physics Research A

journal homepage: [www.elsevier.com/locate/nima](http://www.elsevier.com/locate/nima)

## The test beamline of the European Spallation Source – Instrumentation development and wavelength frame multiplication

R. Woracek<sup>a,\*</sup>, T. Hofmann<sup>b</sup>, M. Bulat<sup>b</sup>, M. Sales<sup>c</sup>, K. Habicht<sup>b</sup>, K. Andersen<sup>a</sup>, M. Strobl<sup>a,c</sup><sup>a</sup> European Spallation Source ESS ERIC, P.O. Box 176, SE-22100 Lund, Sweden<sup>b</sup> Helmholtz-Zentrum Berlin für Materialien und Energie, Hahn-Meitner Platz 1, 14109 Berlin, Germany<sup>c</sup> Technical University of Denmark, Fysikvej, 2800 Kgs. Lyngby, Denmark

### ARTICLE INFO

#### Article history:

Received 12 August 2016

Received in revised form

13 September 2016

Accepted 16 September 2016

Available online 17 September 2016

#### Keywords:

Neutron scattering

Neutron instrumentation

Chopper systems

Wavelength frame multiplication

### ABSTRACT

The European Spallation Source (ESS), scheduled to start operation in 2020, is aiming to deliver the most intense neutron beams for experimental research of any facility worldwide. Its long pulse time structure implies significant differences for instrumentation compared to other spallation sources which, in contrast, are all providing short neutron pulses. In order to enable the development of methods and technology adapted to this novel type of source well in advance of the first instruments being constructed at ESS, a test beamline (TBL) was designed and built at the BER II research reactor at Helmholtz-Zentrum Berlin (HZB). Operating the TBL shall provide valuable experience in order to allow for a smooth start of operations at ESS. The beamline is capable of mimicking the ESS pulse structure by a double chopper system and provides variable wavelength resolution as low as 0.5% over a wide wavelength band between 1.6 Å and 10 Å by a dedicated wavelength frame multiplication (WFM) chopper system. WFM is proposed for several ESS instruments to allow for flexible time-of-flight resolution. Hence, ESS will benefit from the TBL which offers unique possibilities for testing methods and components. This article describes the main capabilities of the instrument, its performance as experimentally verified during the commissioning, and its relevance to currently starting ESS instrumentation projects.

© 2016 Elsevier B.V. All rights reserved.

### 1. Introduction

The European Spallation Source, ESS, that is currently under construction in Lund, Sweden, is expected to deliver first neutrons in 2020. The 5 MW source shall provide the brightest peak flux of any neutron source to date and the time averaged flux will be comparable to the flux of the best continuous high flux reactor neutron sources [1–3]. The existing pulsed spallation neutron sources, including the two most recently built and powerful sources, the Spallation Neutron Source, SNS, in the US [4] and the Japanese Spallation Neutron Source at J-PARC [5] as well as the medium flux spallation sources that have been operational for around 30 years at the Los Alamos Neutron Scattering Center [6] in the US and at the Rutherford Appleton Laboratory [7] in the UK all provide a short neutron pulse. A short pulse duration allows to achieve the best required wavelength resolution by the choice of the length of the instrument and the choice of the moderator, i.e. trading flux for resolution. The long pulse at the ESS enables high efficiency also for those neutron scattering techniques that require

only a relaxed wavelength resolution (5–15% for a majority of applications), such as small-angle neutron scattering (SANS), reflectometry and spin-echo spectroscopy [8]. Moreover, the long pulse allows for very flexible pulse shaping and tunable wavelength resolution that can be adjusted to the instrumental and even to the individual experimental requirements by appropriate disc chopper systems. This enables instrumentation to maximize the efficiency for a broad range of applications combining the flexibility of a continuous source with the efficiency of a pulsed source. In addition, the pulse can be shaped symmetrically which is of particular advantage, e.g. in the case of diffraction. Here, “ideally symmetric peak shapes can be obtained that will allow more precise refinements of both crystal and magnetic structures” [9]. Several neutron instrument types, such as SANS beamlines, reflectometers, diffractometers and imaging stations profit from the opportunity to exploit the full pulse width and its high flux for low wavelength resolution measurements. However, the long pulse approach maintains the opportunity to tune the resolution by cutting the pulse shorter and trading flux correspondingly. The best efficiency is obtained for instruments which are able to work with multiple wavelength frames from each source pulse in a so-called wavelength frame multiplication (WFM) mode [10–12].

\* Corresponding author.

E-mail address: [robin.woracek@ess.se](mailto:robin.woracek@ess.se) (R. Woracek).

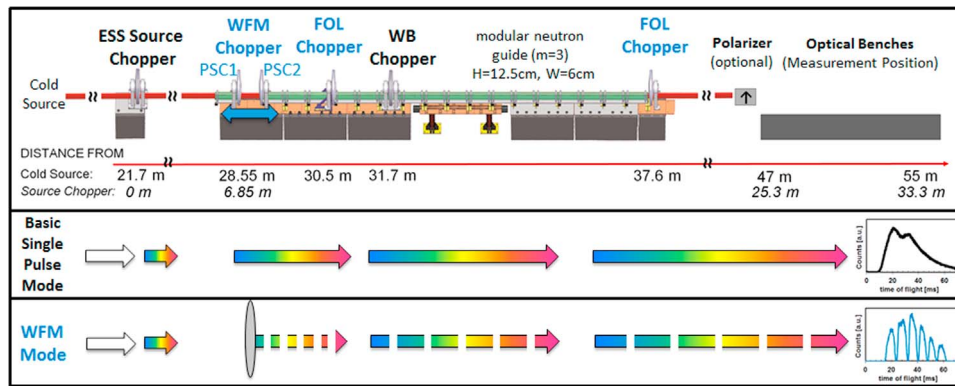


**Fig. 1.** (a) Layout of the test beamline (TBL) with locations of all choppers. The source chopper system, mimicking the ESS source pulse consist of a counter rotating double disc chopper (ESS Source Chopper) and a wavelength band (WB) chopper that is also a double disc chopper. The WFM chopper system consists of two single disc pulse shaping choppers (WFM PSC1 and WFM PSC2), each mounted on a translation stage (optical blind), and a set of two frame overlap (FOL) choppers. (b) Illustration of the basic single pulse mode, where the measurement position defines the wavelength resolution and a continuous spectrum is recorded at the detector. (c) Illustration of the six-fold WFM mode, where the spectrum is divided into sub-frames that are separated in time of flight, but overlap in wavelength.

However, so far no practical experience exists with the experimental realization of such pulse shaping techniques and the related data reduction, i.e. stitching of data from several “sub-frames”.

A dedicated test beamline (TBL) providing a complete WFM chopper system has been designed [11] and installed at the BER II research reactor at Helmholtz-Zentrum Berlin (HZB). The construction was part of the contribution of Germany to the design update phase of the ESS project. The TBL started its “hot” commissioning phase in spring 2015 and is now fully operational.

The TBL provides the ideal infrastructure for a “green field project” such as ESS to investigate novel instrument concepts and test and implement specific hardware and software already during the construction phase. For instance, the ESS will utilize a standardized and integrated control system for all instruments, which is currently under development [13] and will require integration with instrument hardware. The TBL allows for this control system to interface with different beamline components individually while retaining the instrument functionality as a whole. ESS specific components can be quickly integrated as they become available and require testing. Thus the TBL significantly aids the early success of the ESS by providing the opportunity to fully integrate all levels of control and data acquisition well before ESS instruments enter commissioning. Data reduction and analysis routines that are – to some extent – specific for long pulse source instrumentation can already be implemented as well. In particular, the TBL allows to test the WFM mode in different experimental configurations (e.g. diffraction, imaging, reflectometry, SANS) and to develop experimental procedures, experience and specific data reduction (‘stitching’) routines that will be relevant to the corresponding ESS instruments. The availability of testing capabilities at the TBL is a significant factor to provide a fully functional system at ESS at the beginning of operations, helping to save valuable beam time and minimizing delays in scientific production. Moreover, given its high level of flexibility, the TBL is ideally suited to develop novel instrumentation and cutting-edge techniques that can take full advantage of the ESS in the future. These developments will be briefly introduced in this article, while details will be described in corresponding publications.

## 2. Instrument layout

The TBL has been designed to mimic the time structure of the ESS in both, pulse shape and periodicity, by using a counter-rotating double chopper system. Moreover, the instrument has a

sophisticated pulse shaping chopper system installed, in form of wavelength frame multiplication (WFM) choppers that provide six sub-pulses from each source pulse. The TBL is the first instrument that uses a dedicated WFM chopper system, a principle that has first been suggested in Ref. [10]. Hence, many of the instruments at the ESS will benefit from the experience that is gained at the TBL, including method development, data reduction and analysis as well as testing hardware interfaces.

The main parameters of the TBL have already been discussed in Ref. [11] and are summarized in the following for a comprehensive overview. We emphasize that a few changes have been made since the conceptual design phase. A more detailed specification of key instrument components is summarized in the table in the Appendix A.

The TBL has been installed during the ESS design update phase (2010–2013) at HZB [14,15]. In the same period an upgrade project was conducted at HZB aimed at upgrading the cold-neutron instrument suite at BER II. This opportunity was used to install a new supermirror guide ( $m=3$ ) with a large cross-section of  $60 \times 125 \text{ mm}^2$  between the renewed cold-neutron TOF spectrometer (NEAT) [14] and the SANS instrument V4 [16], facing the center of the cold neutron source. The guide, designated as NG2b, starts at a distance of 1.53 m from the cold source as part of the in-pile section. A rotary shutter is installed at a distance of 5 m and the neutron guide continues with curved sections (5 m of  $R_{C1}=1500 \text{ m}$  and 30.45 m of  $R_{C2}=2300 \text{ m}$ ) with the final 5 m being straight, ending at 46.17 m from the cold source. The guide has several gaps where the choppers are positioned as depicted in Fig. 1 and the Appendix A.

The ESS pulse is mimicked by a double chopper at 21.75 m, while a wavelength band chopper (also a double chopper) is installed at 31.7 m that allows separating pulses by defining the wavelength bandwidth. The bandwidth varies between 6.1 Å and 10.2 Å with the distance of the sample position chosen between 47 m and 55 m from the cold source. The maximum possible sample position is located at 60 m from the cold source. The double chopper configuration enables to set a wide range of bandwidths with no lower limit. With this basic chopper system, the wavelength resolution is defined by the instrument length and the burst time which is designed to be identical to the ESS pulse length with  $\tau=2.86 \text{ ms}$ . Since the instrument length, measured from the ESS source pulse choppers, is relatively short compared to the average length of instruments at ESS, the wavelength resolution provided with the ESS source pulse length is relatively low, i.e. 4.2% at 8 Å to 16.6% at 2 Å at 55 m (33.25 m flight path from the source pulse). Such resolution is acceptable for many

**Table 1**  
Example wavelength resolutions that can be obtained using typical values for the parameters at the TBL. Single pulse mode operation is shown for two different burst times (2.86 ms is referred to as basic ESS pulse mode).  $z_0$  is the distance between the WFM choppers PSC1 and PSC2. For the example settings of the WFM mode, corresponding ToF spectra are presented in Fig. 11.

Mode	Spectrum in Fig. 11	Burst time [ms]	Detector position [m]	$L_{\text{tof}}$ [m]	$\Delta\lambda/\lambda$ [%]					
					2 Å	4 Å	8 Å			
Single pulse	X	2.86	47.3	25.55	21.6	10.8	5.4			
		2.86	50.8	29.05	19.0	9.5	4.8			
		2.86	55	33.25	16.6	8.3	4.2			
		0.4	47.3	25.55	3.1	1.5	0.8			
		0.4	50.8	29.05	2.7	1.4	0.7			
		0.4	55	33.25	2.4	1.2	0.6			
WFM	Spectrum in Fig. 11	$z_0$ [mm]			$\Delta\lambda/\lambda$ constant					
					B	140	2.86	47.3	18.75	0.75
					A	427	2.86	47.3	18.75	2.27
					D	140	2.86	50.8	22.25	0.63
					C	427	2.86	50.8	22.25	1.91

neutron scattering techniques, such as reflectometry, SANS and spin-echo encoding. These methods will actually benefit the most from the ESS long pulse as compared to short pulse sources. Some more examples of specific resolution settings that can be achieved at various settings are included in Table 1.

Since many scattering and imaging methods require better wavelength resolution, additional pulse shaping is required as pointed out earlier. The TBL is hence equipped with a wavelength-frame-multiplication (WFM) chopper system that chops the initial pulse into six sub-pulses, generating what is referred to as 'wavelength frames'. The first component in the WFM system is the pulse-shaping chopper (PSC) pair which operates in an optically blind mode [11], meaning that the closing time of the first chopper coincides in time with the opening time of the second chopper, while their distance can be varied by moving them simultaneously along the beam axis. This provides tunable wavelength resolution, which is nevertheless constant over the full wavelength band. In order to avoid overlap between the wavelength frames in time of flight (ToF), two frame overlap (FOL) choppers are installed. Due to the large cross-section of the neutron guide three additional slits ( $5 \times 10 \text{ cm}^2$  between the WFM choppers that is adjustable,  $5 \times 10 \text{ cm}^2$  after the FOL chopper 1 and  $2 \times 10 \text{ cm}^2$  after the FOL chopper 2) are installed in the guide system to reduce contaminant neutron trajectories as discussed in [11].

For polarized neutron experiments, a polarizing S-bender has been installed at the end of the neutron guide. The S-bender is located inside the concrete shielding with a guide field extending outside of the shielding and can be positioned either in or out of the beam remotely.

Downstream of the end of the guide system, which is hosted in a common shielding, optical benches based on item<sup>®</sup> aluminum profiles have been installed and aligned along the beam direction, allowing fixing and aligning components flexibly and efficiently. The benches currently span a length of 6 m, from 47.1 to 53.1 m from the cold source, while the length can be increased up to the 60 m position. The center of the beam is 370 mm above the bench, which can be adjusted if needed. The beam height is 1200 mm above the floor level.

Fig. 1a shows the principal components of the TBL, while Fig. 1b illustrates the operation in the basic single pulse mode, i.e. operating ESS source chopper and wavelength band chopper only. Fig. 1c illustrates the WFM mode. The available space for experimental setups can be seen in Fig. 2. The pictures in Fig. 3 showcase how different experimental setups can be realized at the TBL, underlining the versatility of the instrument.

### 3. Commissioning results

#### 3.1. Beam characteristics

Spectral flux measurements were performed for the basic single pulse mode, while the WFM chopper system was parked in the open position. The source chopper was set to mimic the ESS pulse (2.86 ms pulse length with a repetition rate of 14 Hz) and the wavelength band choppers were set to prevent frame overlap within the repetition rate.

The spectrum and flux were measured with a calibrated  $^3\text{He}$

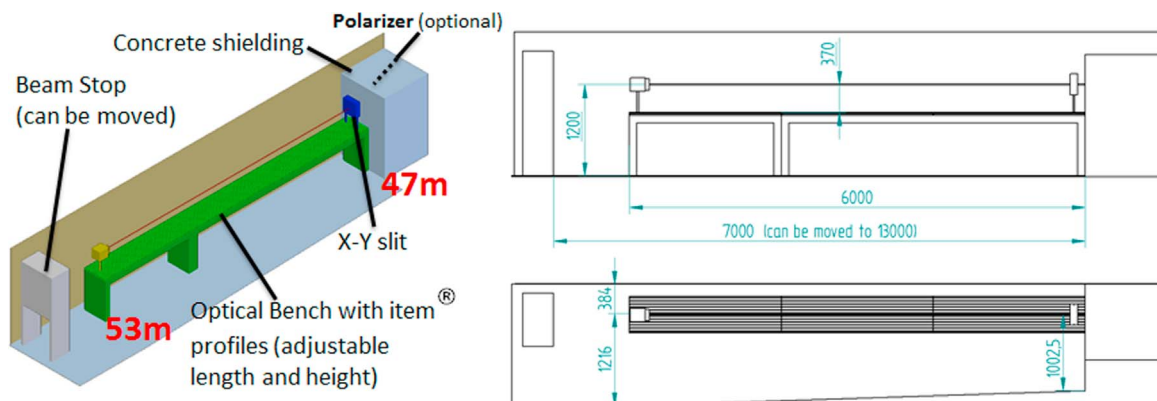


**Fig. 2.** Dimensions of the experimental endstation. A polarizer is installed at the end of the neutron guide, inside the concrete shielding. Motorized X-Y slits allow defining the beam. The optical bench is flexibly adjustable.

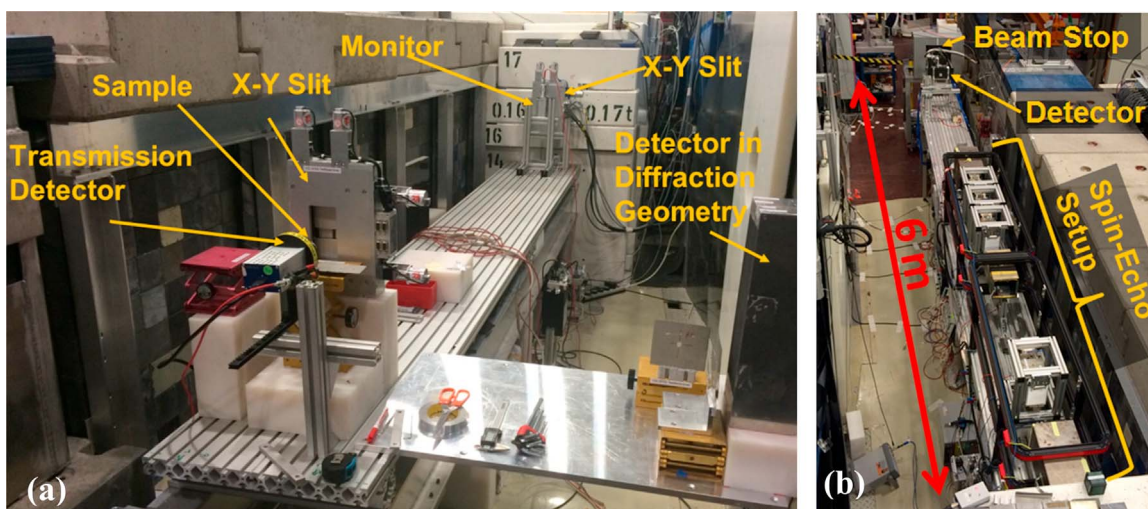


**Fig. 3.** Example usage of the test beamline: (a) experimental setup for powder diffraction with a detector at  $90^\circ$ ; (b) experimental setup for spin-echo experiments, where the beam is polarized at the end of the neutron guide.

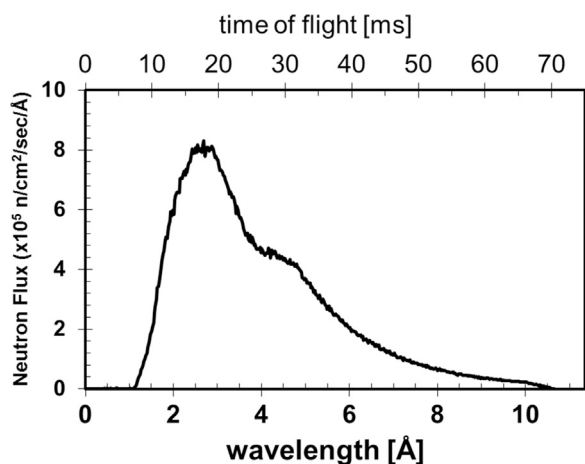


**Fig. 4.** Neutron spectrum at a distance of 47.3 m from the cold source (25.6 m from the source chopper).

beam monitor with a detection efficiency of  $10^{-5}$  at  $1.8 \text{ \AA}$ . The monitor was placed at a distance of 1.1 m behind the end of the neutron guide which is the first accessible position downstream from the concrete shielding. This position corresponds to  $L_{\text{Det}}=47.3 \text{ m}$  from the cold source and a flight path of  $L_{\text{TOF,SP}}=25.6 \text{ m}$  from the source chopper. As the leading edge of

the opening of the chopper pair triggers the start of the detector electronics, a corresponding  $t_0$  time correction needs to be applied to the ToF data when converting to wavelength (see Eq. (1)). The illuminated area was  $2 \times 2 \text{ cm}^2$  defined by a borated slit system that was placed directly in front of the monitor and positioned in the center of the beam (the guide having a cross section of  $6 \times 12.5 \text{ cm}^2$ ). The corrected neutron flux is presented in Fig. 4. The integrated neutron flux is determined as  $3 \times 10^6 \text{ n/cm}^2/\text{s}$ .

The neutron beam size and intensity distribution have been characterized with a scintillator coupled CCD camera system as shown in Fig. 5a. The intensity was further characterized at various detector distances, up to 50.8 m from the cold source. The intensity per area decreases with an increase in distance due to the angular divergence of the beam and about 3% of loss per meter can be attributed to air scattering and absorption. In the presented comparison, the beam was limited to  $5 \times 10 \text{ cm}^2$  by a borated slit system placed at 47.1 m. The vertical divergence of the beam is rather large ( $> 0.25^\circ$ ) while the horizontal divergence is restricted by the three additional narrow slits (see Section 2) in the guide. The visible vertical structures in the beam cross section in Fig. 5a are a signature of the gaps and slits in the guide while the latter introduce a collimation that enables this observation. The same collimation effect causes the horizontal beam width not to change significantly with the distance from the end of the guide (Fig. 6a).

In order to test the real space resolution capability of the basic

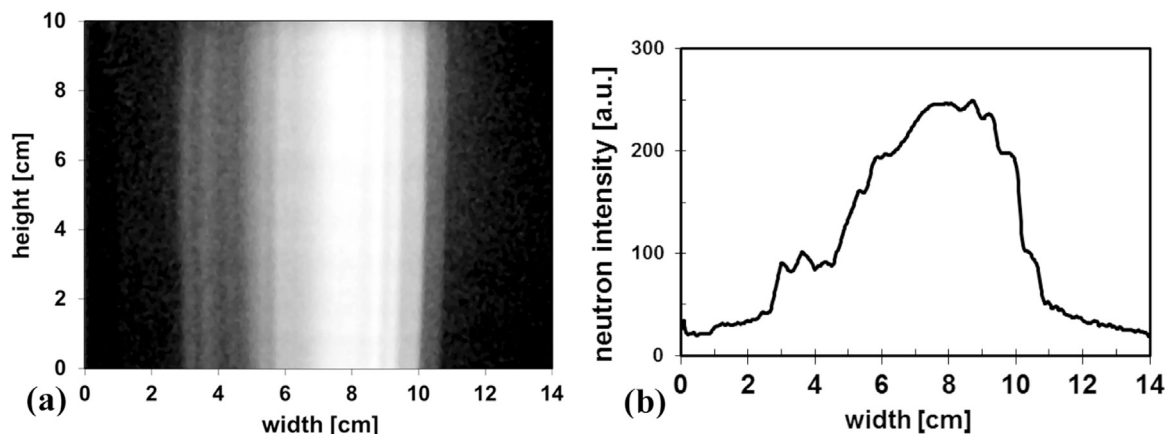


**Fig. 5.** (a) The beam profile at 47.3 m (about 1.1 m after the end of the guide, without any additional slit), recorded with a scintillator-CCD camera. (b) Intensity distribution across the beam profile.

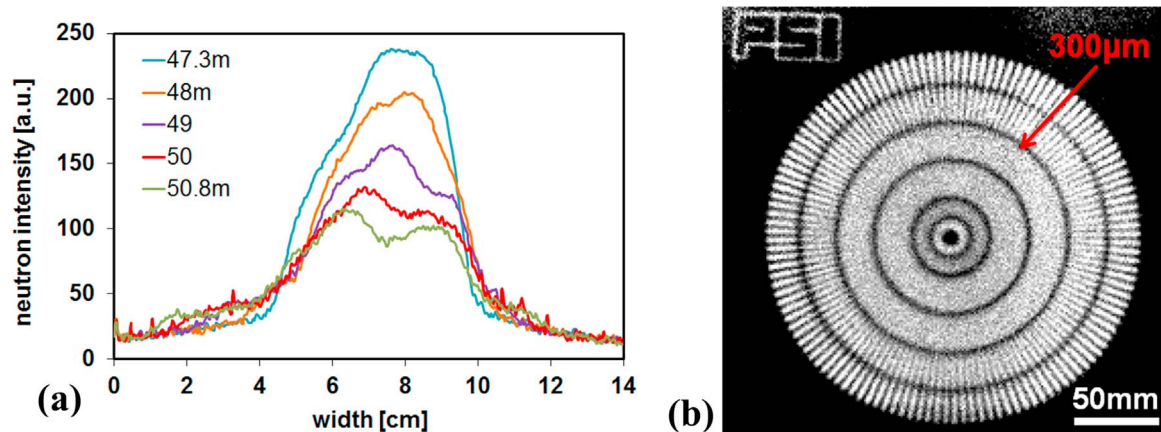


**Fig. 6.** (a) Intensity distribution across the beam profile at increasing detector distances (using a slit that limited the beam to  $5 \times 10 \text{ cm}^2$  after the guide exit). (b) Demonstration of obtainable spatial resolution using a standard resolution mask and a MCP neutron imaging detector.

set-up, a pinhole was introduced by placing a borated slit of 10 mm height and 50 mm width at a distance of 47.1 m and an imaging detector at a distance of 50.8 m. The slit size in the vertical direction was chosen significantly smaller than in the horizontal direction to account for the difference in incident divergence. The corresponding theoretical collimation ratios  $L/D$ , where  $L$  denotes the distance from pinhole to sample position and  $D$  the pinhole dimension, are 370 and 123 in the vertical and horizontal direction, respectively. A position and ToF sensitive imaging detector was installed at the TBL that uses highly neutron-sensitive ( $^{10}\text{B}$  doped) microchannel plates (MCPs) inside a hermetically sealed vacuum tube and operates with a delay line readout. The active area of the detector has a diameter of 40 mm [17]. Using a standard resolution mask [18], spatial features down to twice the pixel size of  $150 \mu\text{m}$  could be resolved. The detector settings in the present example resulted in this relatively coarse pixel size. However, in general the spatial resolution can be improved by another choice of detector parameters.

### 3.2. Characterization of the source pulse

In contrast to short pulse neutron sources, that feature a sharp peak with an extended tail, the long pulse from the ESS will have a distinct pulse shape that rises steeply, and then slowly reaches a plateau, before it decays with the characteristic tail as well. Hence, short and long pulse sources both feature a tail at the end of the pulse that is mainly determined by the moderator properties. In order to mimic the long pulse structure, a double chopper system is well suited, where the characteristic rise is achieved by two different chopper speeds: One chopper opens fast and the second chopper delays the full opening of the beam. The plateau is reached when both choppers are fully open. The slower chopper at the TBL runs at the future ESS source frequency of 14 Hz and has a single window of  $23^\circ$  while the second, counter rotating chopper is operated at 3 times the source frequency, i.e. at 42 Hz and has a window of  $50^\circ$ . The details of the chopper system are described in [11]. The only feature that cannot be replicated properly this way is the decaying tail, which however is of less significance for applications at a long pulse source, in particular because for higher wavelength resolution the pulse can be shaped by choppers adequately.

The source pulse contains neutrons of all energies which will start to propagate with varying speeds, determined by their energies, i.e. wavelengths  $\lambda$ . At the detector which is located at a distance  $L_{\text{Det}}$  from the pulse-defining choppers, the neutrons are separated by their time of flight, defined by:

$$\tau_{\text{TOF}} = \lambda m L_{\text{Det}} / h = L_{\text{Det}} \lambda / 3956 \text{ (}\text{\AA} \text{ m/s)}, \quad (1)$$

where  $m$  is the mass of the neutron and  $h$  is Planck's constant. The wavelength resolution  $\Delta\lambda/\lambda$  at the detector is determined by the burst time  $\tau$  (pulse length) and the time of flight:

$$\Delta\lambda/\lambda = \tau(\lambda)/t_{\text{TOF}}(\lambda). \quad (2)$$

The wavelength resolution hence varies over the wavelength range, where the slower neutrons are separated more than the faster neutrons.

A few possibilities were considered to record the shape of the pulse in order to verify the instrument performance and design parameters. The most straightforward option would be to install a detector directly behind the source chopper itself. However, since there is no space at this position due to the fact that the guide starts right behind the chopper, it was considered to place an incoherent scatterer after the chopper and a detector below it. This option was not implemented however as it would require to open the heavy shielding for the installation of these components, an operation which can only be accomplished during a sufficiently long reactor shut down period. Instead, two other measurement strategies were applied as described below.

#### 3.2.1. Monochromator measurement

The ToF spectrum at the detector position in direct beam geometry is the initial pulse structure convoluted with the ToF spectrum of the wavelength distribution in the pulse. Therefore, when a single wavelength of the initial pulse is selected at the detector position, the pulse shape is convoluted with a delta function, and the pulse shape will directly become apparent. A vivid example is the shape of diffraction peaks at spallation neutron sources. The peaks have an asymmetric profile introduced by the shape of the source pulse which in turn is due to the spallation/moderation process. This peak profile is convoluted with the peak shape produced by the diffraction process itself. However, in the present case with a 2.86 ms long pulse, the contribution of the diffraction peak shape can be neglected.

For the measurement, a pyrolytic graphite monochromator (PG [002]) was placed in the beam at an angle  $\theta=45^\circ$ . Neutrons of a defined wavelength  $\lambda$  (in this case 4.75 Å) are scattered according to Bragg's law,  $\lambda=2d_{hkl}\sin\theta$  towards the detector at  $2\theta=90^\circ$ . The mosaic spread of the monochromator is  $0.8^\circ$ , offering an approximate wavelength resolution of  $\Delta\lambda/\lambda=3\%$ . A  $^3\text{He}$  detector was placed at  $2\theta=90^\circ$  at a distance of 1 m from the monochromator. The detector was operated in event recording mode, where the output trigger signal of source pulse chopper (corresponding to the opening edge of the chopper window) was used to trigger the

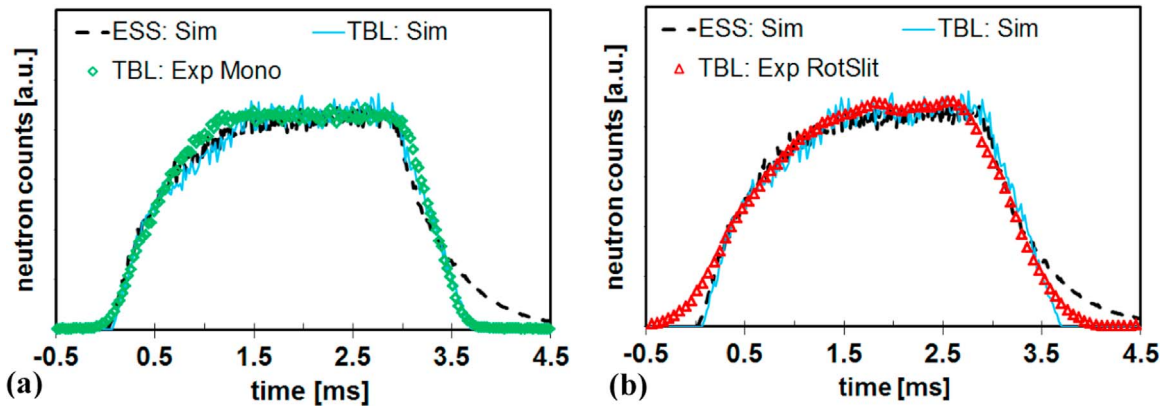


**Fig. 7.** Verification of the pulse shape at the TBL, designed to mimic the pulse produced by the ESS using counter rotating double-disc choppers. VITNESS simulations corresponding to the future ESS source (dashed line) and TBL (blue straight line) are included for comparison. (a) Measurement performed with the PG monochromator and detector at 90°. (b) Measurement performed by utilizing an additional chopper as “slit in time”. (For interpretation of the references to color in this figure legend, the reader is referred to the web version of this article.)

detector electronics. The detector was hence operated at the pulse repetition rate of 14 Hz. More detailed considerations of the accuracy of this approach can be found in Refs. [19,20]. Fig. 7a shows very good agreement of the recorded pulse shape with the design goal for the source pulse profile at the TBL simulated with VITNESS Monte Carlo simulations [11,21].

### 3.2.2. Time-slit measurement

Additionally, a ‘camera obscura’ geometry in ToF (or a ‘ToF pinhole’) was used to project the time structure of the source pulse onto the detector, which was positioned in the direction of the incident beam. The ‘ToF pinhole’ is provided by a fast opening chopper between source and image. Since the wavelength band chopper is actually a double chopper system (with window sizes of 140° and 202°), it could in principle produce a sufficiently fast opening by co-rotating both choppers with a phase to produce a window with the size of the beam cross section. However, although located optimally at about half way between the source choppers and the detector position, the wavelength band chopper cannot turn fast enough (maximum frequency 42 Hz) to produce a sufficiently small time window for a well resolved projection. Hence the WFM chopper pair was utilized for this task. The disks were moved to the minimum distance between each other and the phases were set so that only a small single window was produced, while rotating at the maximum frequency of 70 Hz. Another advantage of this set-up is the remotely controlled slit installed between these choppers, which allows reduce the beam width (in this case 5 mm), improving the projection conditions significantly. The recorded signal – in analogy to a pinhole camera – needs to be inverted and corrected for the “magnification” of the projected pulse width according to  $L_{\text{Source-RotatingSlit}}/L_{\text{Detector-RotatingSlit}}$ . The recorded pulse shape, using the same detector as for the measurement with the monochromator, is shown in Fig. 7b. Good agreement is obtained when comparing the results of the two measurement techniques. The tails at the beginning and the end of the pulse observed with the ‘ToF pinhole’ technique are attributed to additional broadening in time due to the finite width of the chopper transmission function.

### 3.3. Versatility of pulse lengths at the TBL

Besides its main design purpose to mimic the ESS time structure, the setting of the double disc source pulse chopper system can be varied such that pulse durations longer or shorter than the ESS source pulse can be realized. Examples of possible settings can be found in the Appendix A. This enables even more versatility of the TBL. For

instance, when the wavelength frame multiplication mode is tested with its high wavelength resolution in the six sub-frames of the full wavelength band, it is useful to compare the experimental results to a measurement with a continuous wavelength band with the same (high) resolution. An example of the shortest achievable pulse width is presented in Fig. 8, having an approximate FWHM of 400  $\mu\text{s}$ . Examples of possible experimental configurations and the achievable range in wavelength resolution are included in Table 1.

### 3.4. Wavelength frame multiplication

The basic principle of wavelength frame multiplication (WFM) was proposed in Refs. [10,22] and practical aspects and specific designs including Monte Carlo simulations of real systems are discussed in Refs. [11,12,23]. First proof-of-principle experiments were undertaken at a continuous reactor source and have demonstrated the feasibility of the approach [24]. The idea to combine WFM with the principle of optical blind choppers for constant wavelength resolution and the specific design procedure for an optical blind WFM system is described in detail in Ref. [11]. This combination was applied in the design of the TBL.

The principle layout and functionality of the chopper system for the TBL is shown in the ToF diagram that is reprinted here in Fig. 9. The WFM Pulse Shaping Choppers (WFM PSC) operate in optical blind mode, which requires individual windows for each wavelength frame. As a consequence the maximum achievable chopper frequencies are limited. The ToF starting point  $t_{0n}$ , i.e. the effective pulse source position of each wavelength frame, for an

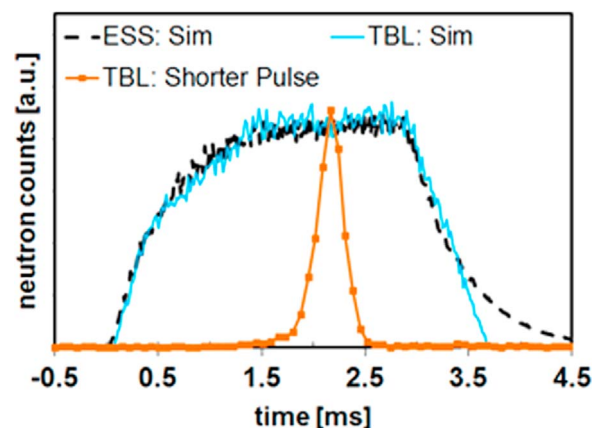


**Fig. 8.** Example of a short pulse produced with counter rotating double-disc chopper. The data was recorded using a PG monochromator as described in Section 3.2.1.

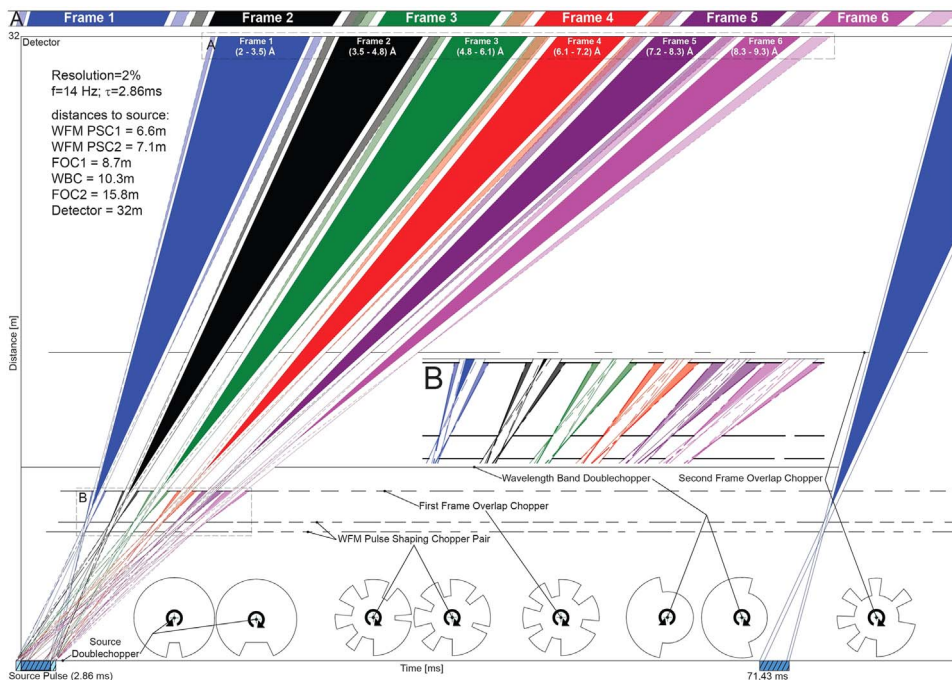


**Fig. 9.** (Reprinted from [11]) ToF diagram for the TBL. The locations and disc profiles of the choppers are shown. The insets A and B provide magnified views of the detector position and the pulse shaping, respectively. The dark colored areas together with the non-colored next to them display the mean of the desired wavelength bands of each sub-frame, while the consecutive semi-transparent areas display potential overlap fractions originating in the pulse broadening in time. These are partly suppressed at the frame overlap choppers or otherwise arrive in non-used time fractions at the detector. (For interpretation of the references to color in this figure legend, the reader is referred to the web version of this article.)

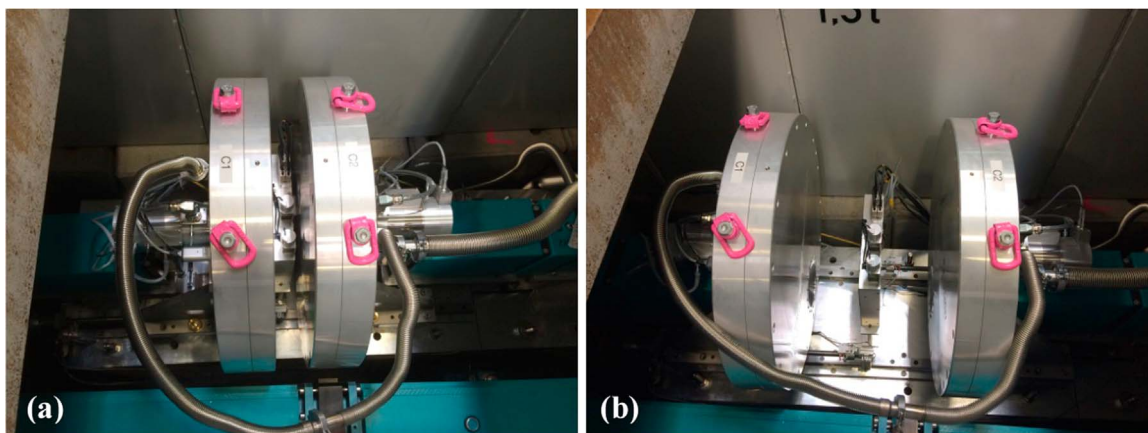


**Fig. 10.** The WFM chopper system on the linear stages with the slit system in the center. (a) Showing the arrangement with the minimum distance between the two choppers, yielding the highest resolution. (b) Showing the arrangement with the maximum possible distance, yielding higher intensity at lower resolution.

optical blind chopper system, is given at the position half way between the first (WFM PSC1) and the second (WFM PSC2) pulse shaping chopper (more detailed discussion in 3.4.2). In the case of the test beamline, the center between the choppers is at a distance of 6.85 m away from the source chopper (28.55 m from the cold source). Note that the ToF reference time  $t_{on}$  of the WFM system is individual to each frame. The wavelength resolution can be tuned by changing the distance  $z_0$  between the choppers. Each chopper can be individually translated along the beam axis, keeping the ToF reference times  $t_{on}$  unchanged. The minimum and maximum distances that can be achieved for the WFM PSC at the TBL are  $z_{0min} = 140$  mm and  $z_{0max} = 427$  mm, respectively. These two extreme cases are shown in Fig. 10.

#### 3.4.1. Tuning the resolution

In order to test the performance of the WFM system, a  $^3\text{He}$  detector operated in event recording mode was placed in the direct

beam. By varying the chopper settings and the detector position, several instrument configurations with different wavelength resolutions were investigated. The detector acquisition was started with the opening of the ESS source pulse chopper and data recorded in histogramming mode. The corresponding ToF spectra presented in the following are using the time  $t_{sourceChopperOpening}$  as the reference time, i.e. the point in time of the opening of the choppers which mimic the ESS source pulse. The beam size was restricted to a size of  $5 \times 5$  mm<sup>2</sup> using a slit system positioned in the center of the full beam cross section at 47.1 m from the cold source.

Fig. 11a depicts four ToF spectra that were recorded using the maximum and minimum chopper distances  $z_0$  and two different detector positions,  $L_{Det1} = 47.3$  m and  $L_{Det2} = 50.8$  m from the cold source. The flight paths  $L_{TOF}$  from the center of the WFM chopper pair to the detector position, are hence given as  $L_{TOF|WFM} = 18.75$  m and  $L_{TOF2|WFM} = 22.25$  m. The wavelength resolution is given by  $\Delta\lambda/\lambda =$

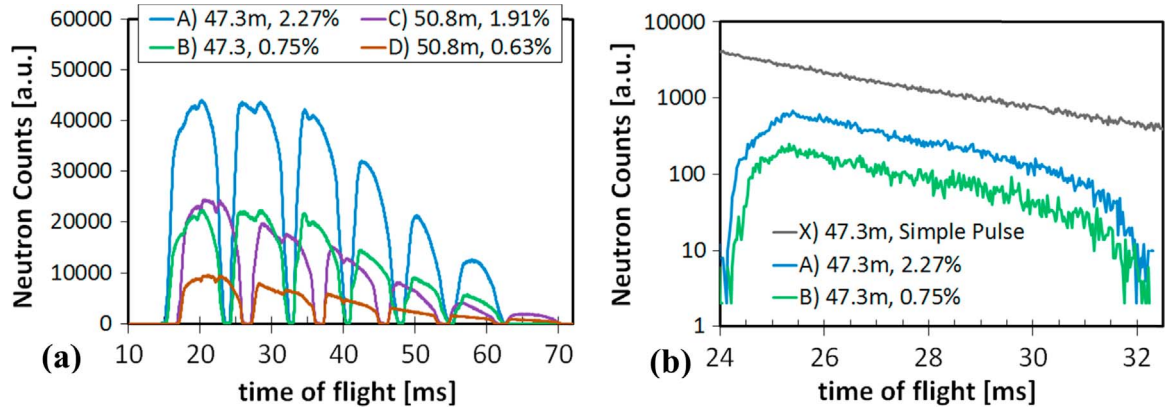


**Fig. 11.** (a) Four example spectra of the incident beam, recorded by placing the detector at two different distances on the optical bench and using the highest and lowest resolution achievable with the optical blind WFM chopper system. The resolutions for the presented settings are included in Table 1. (b) Comparison of measured intensities using the basic ESS pulse mode (no WFM) or the WFM mode in highest and lowest resolution setting for a detector distance of 47.3 m.

$Z_{0\text{min}}/L_{\text{TOF}}$  and is presented in Table 1 for the cases shown in Fig. 11. The differences in the overall flight time for the different detector distances are evident. Also, the neutron intensity varies with detector distance and with the resolution chosen. The flux at the same detector position scales linearly with the resolution as expected. For the two WFM settings presented in Fig. 11b the intensity differs by a factor of approximately 3. The intensity at different detector distances is obviously influenced not only by the resolution, but also by the beam divergence and air scattering losses along the final flight path.

For a quantitative comparison of the neutron flux versus resolution for the basic ESS single pulse mode (without WFM) and two distinct WFM modes (highest and lowest resolution setting), care was taken to prevent saturation of the detector, as had been observed before in particular in the basic ESS single pulse mode. Therefore beam absorbers, in the form of borosilicate glass plates with 12.5%  $\text{B}_2\text{O}_3$  content and a thickness of 7 mm, were added at the slit position (this applies only to the data presented in Fig. 11b). This ensured quantitative count rates of the detector system within its dynamic range for all resolution settings, but also resulted in the strong absorption of longer wavelength neutrons by the borated glass. For the comparison presented

here, the detector was placed at a distance  $L_{\text{Det1}} = 47.3$  m from the cold source. The flight path  $L_{\text{TOF}}$  in the case of the single pulse mode is  $L_{\text{TOF1SP}} = 25.6$  m and measured from the position of the ESS source pulse chopper, while in the case of the WFM mode  $L_{\text{TOF1WFM}} = 18.75$  m is measured from the center of the WFM chopper pair. As mentioned above, the flux should scale linearly with the resolution. In the basic ESS pulse mode, however, the resolution naturally varies over the wavelength band while it remains constant over the wavelength range in the WFM mode. Fig. 11b presents a detailed comparison in the ToF range between 24 and 32 ms, which is within the second wavelength frame of the standard WFM settings. Comparing the flux at 27 ms, a factor of approximately 4.7 between the basic ESS pulse mode and the WFM mode with a resolution  $\Delta\lambda/\lambda = 2.27\%$  is found. This agrees with the expected gain in resolution: A ToF of 27 ms corresponds to roughly  $4 \text{ \AA}$ , where the resolution in the basic ESS pulse mode is  $\Delta\lambda/\lambda = 10.8\%$  implying a factor of 4.8. Corresponding agreement is found across the whole ToF range. Comparing the flux of the lowest and highest WFM resolution setting, the factor of almost exactly 3 over the wavelength band is found which again agrees well with the gain in resolution from  $\Delta\lambda/\lambda = 2.27\%$  to  $\Delta\lambda/\lambda = 0.75\%$ . The effect of the different resolutions is illustrated by application examples in Section 4 of this article.

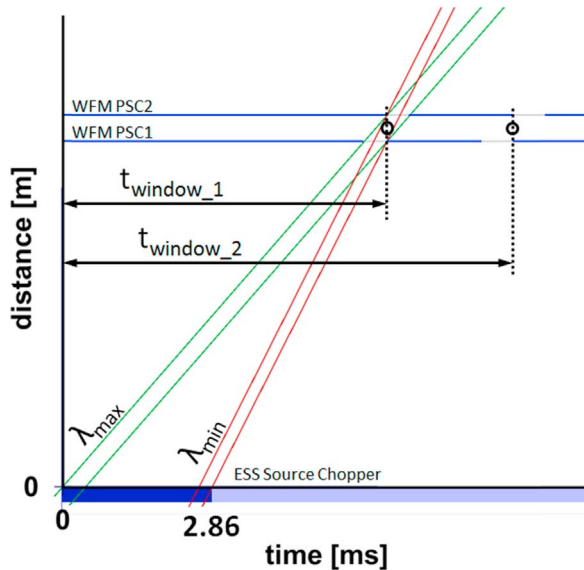


**Fig. 12.** Illustration of the start of the pulses produced by the WFM chopper pair (indicated by a black circle), situated in the center of the pulse for the longest (green lines) and shortest wavelengths (red lines). If for example the opening of the ESS pulse triggers the detector electronics, as in the presented examples, each (of the six) time frames has to be shifted by  $t_{\text{window}_n}$ . (For interpretation of the references to color in this figure legend, the reader is referred to the web version of this article.)

### 3.4.2. Conversion from ToF to wavelength

Using spectrum D of Fig. 11a (recorded at a distance of 50.8 m and the highest resolution setting) as an example, the conversion from the ToF at the detector position to the wavelength scale shall be illustrated. Every individual WFM time frame of the six frames in total at the TBL has its very own ToF reference time  $t_{0n}$ , i.e. the time when the two WFM choppers transmit a pulse of a specific frame  $n$ . More specifically,  $t_{0n}$  is the point in time when the burst times for all wavelengths of one frame are identical. In space this point coincides with the center position between the two pulse shaping choppers (WFM PSC1 and WFM PSC2) as indicated with a black circle in Fig. 12. In time this point coincides in an optical blind chopper system with the closing time of the first and the opening time of the second chopper.

However, the spectrum presented in Fig. 13a is plotted using the time  $t_{\text{SourceChopperStart}}$  as the reference time, i.e. the starting point in time of the opening of the ESS source pulse mimicking chopper pair, which is also triggering the detector. Hence, each individual wavelength frame, corresponding to the six chopper windows  $n = 1 \dots 6$ , has to be shifted by a time offset  $t_{\text{window}_n}$  in order to align it to the reference time  $t_{0n}$ . It can be seen from Fig. 12, that this time offset corresponds to the time that passes between the start of the ESS source pulse and the closing time of the associated window of WFM PSC1 (i.e. opening time of the associated window of WFM PSC2). Besides the distance between the ESS source chopper and the WFM pulse choppers it also depends on the phase and frequency setting of



the WFM pulse shaping choppers and can be determined accordingly for every frame. However, once the offset for the first frame is determined, the time shift between each subsequent frame only involves the frequency. Thus the required time shifts between two consecutive can simply be calculated from the time interval that passes between the central opening times of the individual windows, defined by:

$$t_{\text{ShiftWindow}_n} = \left[ (\theta_{\text{WFMPC1window}_{n+1}} - \theta_{\text{WFMPC1window}_n}) \cdot \frac{f}{360} + (\theta_{\text{WFMPC2window}_{n+1}} - \theta_{\text{WFMPC2window}_n}) \cdot \frac{f}{360} \right] / 2. \quad (3)$$

Here, the angle  $\theta$  (in units of degrees) corresponds to the center position of each window and  $f$  is the rotation frequency of the chopper in Hertz. For example, the offset time for the second frame is given as:

$$t_{\text{Window}_2} = t_{\text{ShiftWindow}_2} + t_{\text{Window}_1} = \left[ (148.14^\circ - 89.205^\circ) \cdot 70 \text{ Hz} / 360 + (133.75^\circ - 70.535^\circ) \cdot 70 \text{ Hz} / 360 \right] / 2 + t_{\text{Window}_1} = 2.42 \text{ ms} + t_{\text{Window}_1} \quad (4)$$

To compare the analytical values derived from the design parameters, calibration measurements were performed by using characteristic, well-known, polycrystalline materials in front of the detector producing Bragg edges at well-defined wavelengths in the transmission spectrum. Materials that were used include face-centered-cubic and body-centered-cubic iron as well as graphite powder (see also Section 4 of this article). The calculated time offset values and the experimentally determined quantities were in close agreement. Slight variations were observed. A maximum difference of 0.058 ms was obtained for the 2nd frame which is equal to a difference of  $\Delta\lambda \approx 0.01 \text{ \AA}$  at the utilized settings corresponding to approximately  $\Delta\lambda/\lambda = 0.25\%$  at  $4 \text{ \AA}$ , well below the wavelength resolution and hence verifying the system specifications.

The spectrum with time offset corrections applied is presented in Fig. 13b. The measured intensity at time channels between the frames is discarded. The start and end of frames is defined through the geometry, rotation speed and flight path. For practical reasons, the start and end of each frame have so far been determined empirically from the measurements. As can be seen in Fig. 13b, in contrast to Fig. 13a, the ToF of neighboring frames overlap after the  $t_0$  correction, which means that the wavelength bands of neighboring frames overlap. The time channel data is rebinned to match the chosen time resolution. The resulting data are then added such that the intensities in the overlapping regions are added together. From there on it is a simple ToF to wavelength conversion (see Eq. (1)) using the distance  $L_{\text{TOF}}$  from the center of the WFM choppers (location of the six WFM source pulses) to the detector position to produce the continuous wavelength spectrum, as shown in

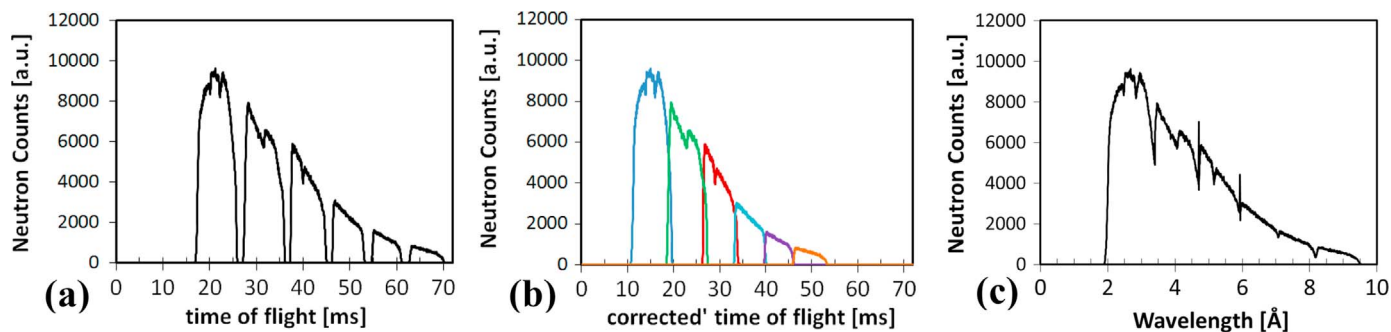


Fig. 13. Conversion from the as-recorded data into a continuous ToF spectrum, using spectrum D of Fig. 11a as an example. (a) For the as-recorded data the wavelength frames are separated in ToF at the detector position. (b) Shifting each frame according to the opening times of the corresponding chopper windows, a continuous ToF spectrum is obtained. (c) The final continuous wavelength spectrum.

Fig. 13c. Finally, the conversion allows comparing the WFM spectra with the basic ESS pulse mode spectrum in Fig. 14.

Even though the WFM chopper system is optimized for certain wavelengths (starting with the first frame at  $2 \text{ \AA}$ ), the system is robust enough to shift the frames by about half their width by delaying the opening times using a different phase offset between the WFM chopper system and the source chopper system. In particular this allows placing the overlap regions between the frames at different wavelengths, and basically to any desired wavelength with respect to two consecutive frames. This allows investigating any potential or suspected perturbation effects on data in the stitching region. An example is shown in Fig. 15 where two spectra, recorded with different phase offsets of the WFM choppers with respect to the source chopper, are shown, while for both the maximum chopper distance  $z_{\text{max}}$  and a detector distance of  $50.8 \text{ m}$  were used.

### 3.5. Polarized option

A polarizing S-bender, containing 400 wafers that are coated with polarizing Fe-Si supermirrors with  $m=3$  and an absorption layer made of an anti-reflecting layer of Gd and Si including a Gd layer with  $1 \mu\text{m}$  thickness, can be moved into the beam by a vertical linear slide and can be aligned via a remote controlled rotation stage. The device has an active area of  $60 \text{ mm}$  width and  $125 \text{ mm}$  height. In addition to the spin-selective absorbing properties of the device, the beam is also slightly deflected to one side. The corresponding intensity distribution at a distance of  $47.3 \text{ m}$  is presented in Fig. 16.

The polarization was characterized at another instrument using a polarized monochromatic ( $4.9 \text{ \AA}$ ) beam and the weighted

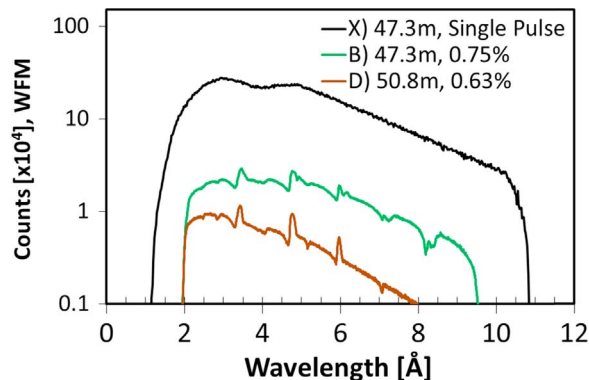
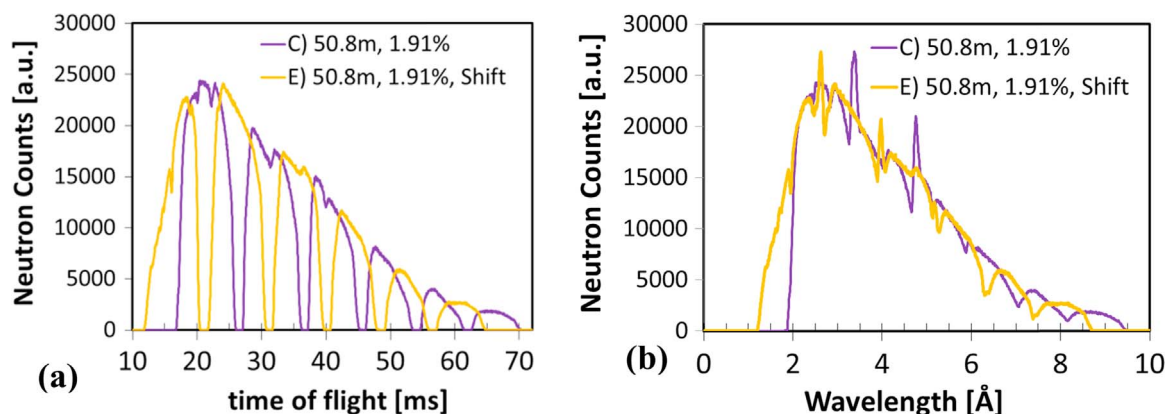
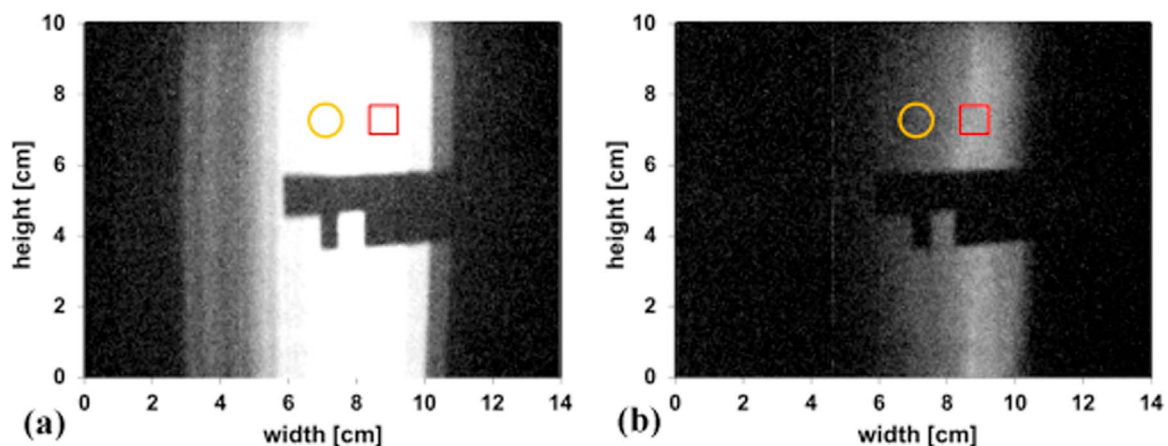


Fig. 14. Comparison of the continuous wavelength spectra for the high resolution WFM settings at  $47.3 \text{ m}$  (green curve) and  $50.8 \text{ m}$  (brown curve). The first wavelength frame starts at  $2 \text{ \AA}$ . The corresponding ToF spectra are shown in Fig. 11a. Also included is the continuous wavelength spectrum that is obtained in the basic ESS pulse mode (black curve). (For interpretation of the references to color in this figure legend, the reader is referred to the web version of this article.)



**Fig. 15.** (a) The frames can be 'moved' by adjusting the delay between the opening of the source chopper and the opening of the WFM chopper windows. (b) This allows placing the overlap regions between two frames at different wavelengths.



**Fig. 16.** The intensity beam profile at 47.3 m (about 1.1 m after the end of the guide) (a) without polarizer and (b) with polarizer. The intensity in the area marked with the red square is 44% of the intensity without the polarizer, while it is 24% in the area marked with the yellow circle. Note: The shaded area results from an absorbing mask that was positioned for a reference. (For interpretation of the references to color in this figure legend, the reader is referred to the web version of this article.)

polarization was determined to be 98.7%. At the TBL, the polarization at the detector was measured during the course of an experimental campaign with a specific set-up. This involved a 3 m guide field and a spin flipper positioned between the polarizer and a compact polarizing bender without an absorption layer, but instead using an independently adjustable collimator to suppress the non-reflected transmitted spin state. The polarization was measured for the basic single ESS pulse mode covering the full design wavelength range (Fig. 17). The resulting values vary between 50% and 80% from 1.8 Å to 9 Å reaching 70% at 2 Å and 80% from 3.5 Å and then remain constant up to 9 Å. In another measurement campaign, involving  $^3\text{He}$  analyzers, the incident beam polarization by the S-bender was determined to be larger than 97% for all wavelengths up to 7 Å.

#### 4. Commissioning of resolution settings by Bragg edge transmission measurements

In order to demonstrate the capabilities of the tunable wavelength resolution with a vivid example, a polycrystalline sample of low carbon steel (BCC structure) with a thickness of 10 mm was placed in front of the detector. The same  $^3\text{He}$  detector as described before was used. The data presented in this section is complementary to the data shown Section 3.4 where no sample was used. Spectra were recorded for the two WFM chopper settings corresponding to the maximum and minimum resolution as well as for the basic single ESS pulse mode. The crystalline structure of the sample gives rise to Bragg scattering and leads to Bragg edges

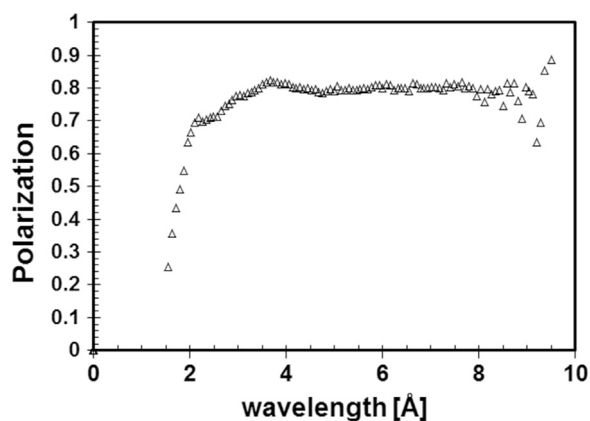


**Fig. 17.** The polarization at the detector position of 51 m measured with a 3.5 m long guide field and a spin flipper installed behind the S-bender. A bender-collimator combination was used as the spin analyzer.

in the transmission spectrum. These Bragg edge patterns can – in analogy to diffraction patterns – be used in imaging experiments for the determination of crystalline phase and lattice strain [25,26] with simultaneous spatial resolution. An example of a similar chopper setup for a continuous source that was used to determine lattice strain under tensile loading can be found in [27]. To obtain the 'transmission spectrum', the 'sample spectrum' is normalized by the 'open beam spectrum' measured without a sample.

The results are shown in Fig. 18a for the high resolution setting

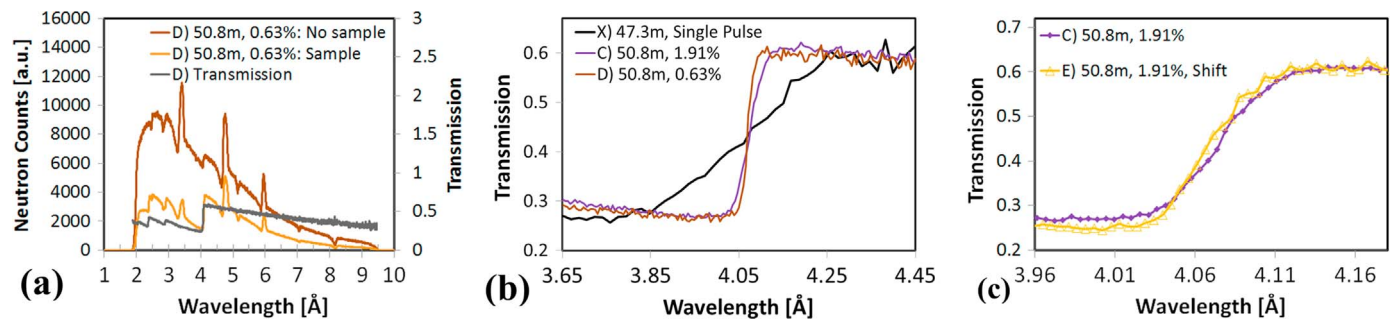


**Fig. 18.** (a) Placing a BCC-iron sample in front of the detector produces characteristic Bragg edges in transmission. The transmission spectrum can be obtained by normalizing the spectrum with sample by the spectrum without sample. (b) Comparison of the different wavelength resolutions for three different operation modes, where the basic ESS pulse mode provides the coarsest resolution resulting in a smearing of the Bragg edge. The highest resolution setting produces the sharpest Bragg edge as expected. (c) By choosing a different phasing of the choppers, the Bragg edge was shifted to be partly at the end of the 2nd frame and partly in the beginning of the 3rd frame. The transmission spectrum after the data reduction and stitching shows good agreement between spectrum C and E and hence demonstrates the functionality of the WFM approach.

recorded at  $L_{\text{Det}}=50.8$  m ( $L_{\text{TOFWFM}}=22.25$  m, spectrum D), where the two measured spectra as well as the normalized transmission spectrum are shown. It can be seen that the sharp intensity peaks, occurring in the frame overlap regions of the spectra, vanish in the normalization and are hence not present anymore in the resulting transmission spectrum.

Fig. 18b depicts the Bragg edge corresponding to the (110) lattice plane family for the high and low resolution WFM setting with the detector at  $L_{\text{Det}}=50.8$  m as well for the basic ESS pulse mode, where the detector was placed at  $L_{\text{Det}}=47.3$  m (lowest wavelength resolution). The differences in wavelength resolution between the three spectra are apparent when comparing the slope of the Bragg edge, which is more smeared when the resolution is coarser. An example with practical application of this effect is presented in [28].

A particular strength of the WFM mode is that a broad continuous wavelength band can be covered with high wavelength resolution at a long pulse source. However, the regions where the frame overlap in wavelengths occurs are potentially prone to artifacts and systematic errors. The verification that the overlap regions do not introduce any artifacts is crucial in order to ensure the correct operation and applicability of such a chopper system. For this purpose, the transmission spectra were recorded using the chopper settings introduced in Fig. 15, where the frames were shifted in spectrum C as compared to spectrum E. Fig. 18c again shows the Bragg edge corresponding to the (110) lattice plane family for both settings, located at around 4.05 Å. While this particular wavelength is located in the middle of the second frame for spectrum C, for spectrum E it is located at the end of the second frame and at the beginning of the third frame, i.e. in the overlap region. It can be seen in Fig. 18c that the transmission spectra and the Bragg edge are basically identical for the two settings, demonstrating the correct operation of the WFM system in this configuration.

## 5. Summary and conclusion

The dedicated ESS test beamline at HZB has started operation and the commissioning of the instrument has shown that it performs according to the design goal. The instrument is highly flexible in terms of experimental setups and a wide selection of optional beamline components is available. These components, e.g. detectors and beam monitors, slits, power supplies, motion stages, etc., can be utilized in various configurations for setups adapted to the measurement task. For specific setups additional equipment can be added and implemented on demand with a high flexibility. This infrastructure showcases the strength of the TBL to serve its two major purposes in being a platform for integration and development of beamline components (hardware and software) that are relevant to ESS and to undertake dedicated development of advanced neutron scattering techniques.

Currently, the TBL can be fully controlled via the control system CARESS provided by the HZB and in parallel via NICOS [29] that is under consideration to be used at ESS. This approach allows a step-by-step integration of components into an ESS framework, eventually also via EPICS [30], without sacrificing the functionality of the TBL, but rather constantly adding to its performance. By performing method development tailored to long pulse sources, the specific needs and requirements for the associated hardware and software become apparent during such measurements and can be addressed accordingly.

Within the first six months of operation, the TBL has successfully served method and component development in areas including WFM diffraction and associated data reduction, ToF imaging detector tests and development [17], diffraction and spectrometer detector tests and associated readout development, PASTIS  $^3\text{He}$  polarization analyzer tests [31], Larmor encoding techniques, such as spin-echo modulated SANS [32–34], ToF wavelength-resolved dark field imaging [35–37] and Bragg-edge transmission analysis [38–40]. Details and results of these experiments will be published elsewhere.

In conclusion, the TBL at HZB as a dedicated ToF testing facility of ESS will play a significant role for the early success of ESS. It supports the necessary technology development required for construction and enables acquiring the experimental expertise required at the start of ESS instrument operation. Apart from advancing the state-of-the-art in neutron methods with a focus on the ESS long pulse source, the test beamline also serves to mitigate the risks associated with a “green field” project.

## Acknowledgments

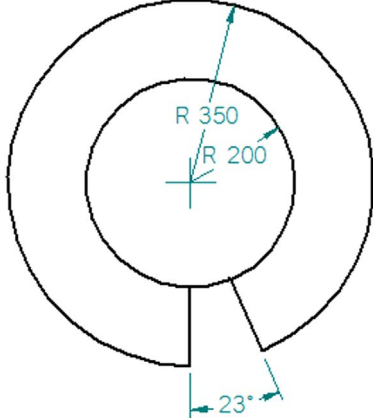
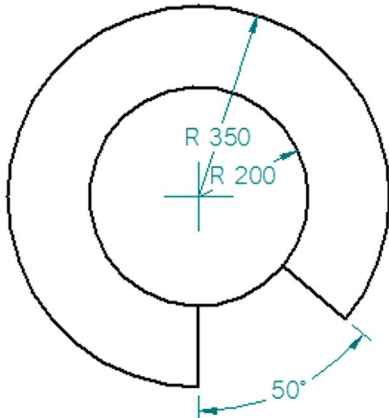
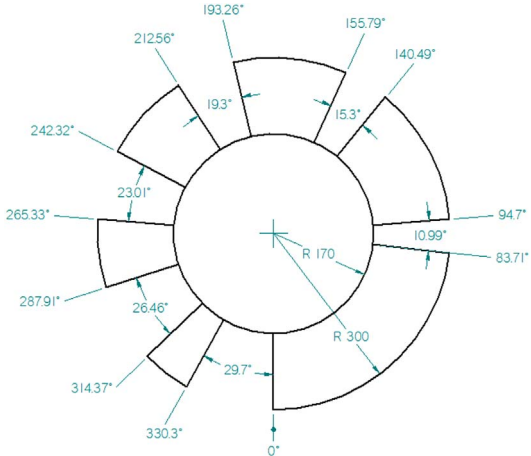
We greatly appreciate the support from HZB staff, especially R. Kischnik, M. Straschewski, G. Steiner, W. Graf, B. Urban, H.J. Bleif, T. Wilpert, L. Rossa, H. Gast and A. Brandt, besides many others. We would like to acknowledge the contributions to data reduction by J. Taylor (ESS/DMSC) and the efforts for the NICOS integration supported by M. Wedel and D. Brodrick (DMSC/ESS) as well as O. Arnold, F. Akeroyd, M. Hart (RAL/ISIS) and J. Krueger (FRM II). Furthermore, we greatly value the kind support for the integration of a PSD detector with ToF capability (DENEX) by G. Nowak, C. Jacobsen, J. Plewka and J. Burmester (Helmholtz-Zentrum Geesthacht). The synergies of testing ToF (imaging) detectors while subsequently using them for an experiment are apparent and we would like to thank A. Tremsin (UC Berkeley), O. Merle (ProxiVision) and A. Oelsner (Surface Concept) for their cooperation and discussions.

## Appendix A

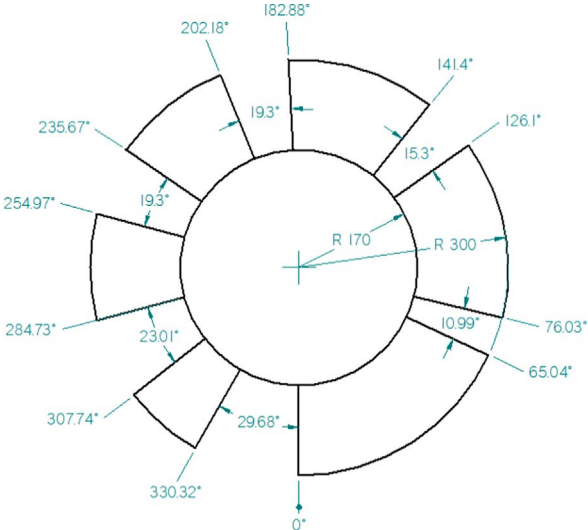
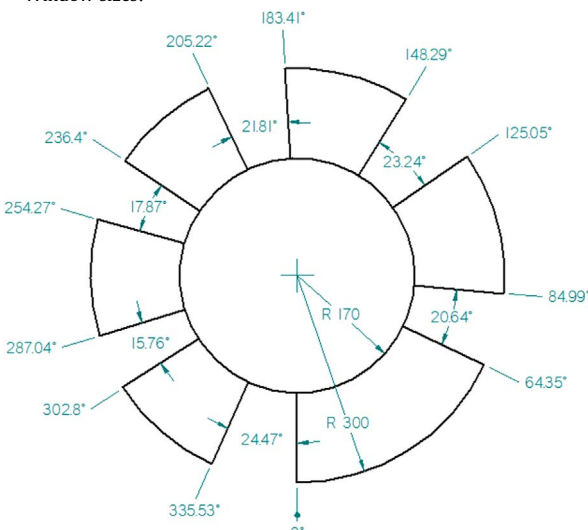
See Table A1.

**Table A1**

The layout of the ESS test beamline is summarized in the following table: .

Component	Distance to cold source [m]	Distance to source chopper [m]	Description
1 Cold source	0	–	
2 Guide	–	–	Inpile part straight, followed by curved sections (R=1500 m and R=2300 m)
3 Source Chopper Disc 1	21.7	0	<ul style="list-style-type: none"> <li>Window size: 23°, d=700 mm</li> </ul>  <ul style="list-style-type: none"> <li>Normal speed: 14 Hz</li> <li>Rotation (viewing from cold source): CW</li> <li>Selectable Speeds: 7 Hz, 8.4 Hz, 10.5 Hz, 14 Hz, 21 Hz, 42 Hz</li> </ul>
4 Source Chopper Disc 2	21.7	0	<ul style="list-style-type: none"> <li>Window size: 50°, d=700 mm</li> </ul>  <ul style="list-style-type: none"> <li>Normal speed: 42 Hz</li> <li>Rotation (viewing from cold source): CCW</li> <li>Selectable Speeds: 7 Hz, 8.4 Hz, 10.5 Hz, 14 Hz, 21 Hz, 42 Hz</li> </ul>
5 Guide	–	–	L=6.5 m, m=3, curved (r=2300 m), H=12.5 cm, W=6 cm
6 WFM Chopper Disc 1	28.3	6.64	<ul style="list-style-type: none"> <li>Window sizes:</li> </ul>  <ul style="list-style-type: none"> <li>d=600 mm</li> <li>Normal speed: 70 Hz</li> <li>Rotation (viewing from cold source): CW</li> <li>Selectable Speeds: 14 Hz, 28 Hz, 42 Hz, 56 Hz, 70 Hz</li> </ul>

**Table A1** (continued)

Component	Distance to cold source [m]	Distance to source chopper [m]	Description
7 Slit	28.55	6.85	Adjustable slit system common setting: H=10 cm, W=5 cm
8 WFM Chopper Disc 2	28.8	7.06	<ul style="list-style-type: none"> <li>Window sizes:</li> </ul>  <ul style="list-style-type: none"> <li>d=600 mm</li> <li>Normal speed: 70 Hz</li> <li>Rotation (viewing from cold source): CW Selectable Speeds: 14 Hz, 28 Hz, 42 Hz, 56 Hz, 70 Hz</li> </ul>
9 Guide	–	–	L=1.5 m, m=3, curved (r=2300 m), H=12.5 cm, W=6 cm
10 Frame Overlap Chopper 1	30.5	8.8	<ul style="list-style-type: none"> <li>Window sizes:</li> </ul>  <ul style="list-style-type: none"> <li>d=600 mm</li> <li>Normal speed: 56 Hz</li> <li>Rotation (viewing from cold source): CW Selectable Speeds: 14 Hz, 28 Hz, 42 Hz, 56 Hz, 70 Hz</li> </ul>
11 Slit	–	–	Fixed slit to prevent frame overlap H=10 cm, W=5 cm
12 Guide	–	–	L=1 m, m=3, curved (r=2300 m), H=12.5 cm, W=6 cm

**Table A1** (continued)

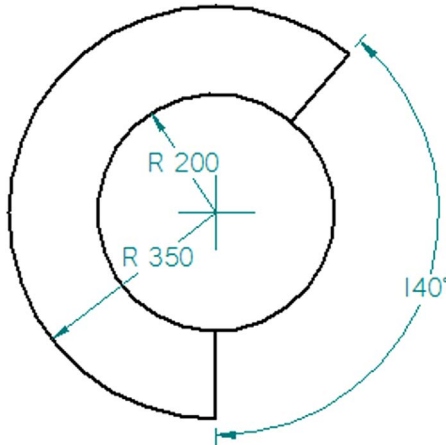
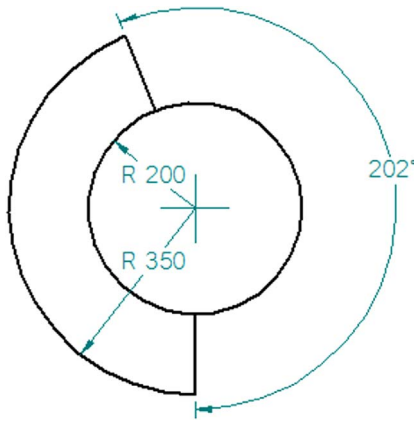
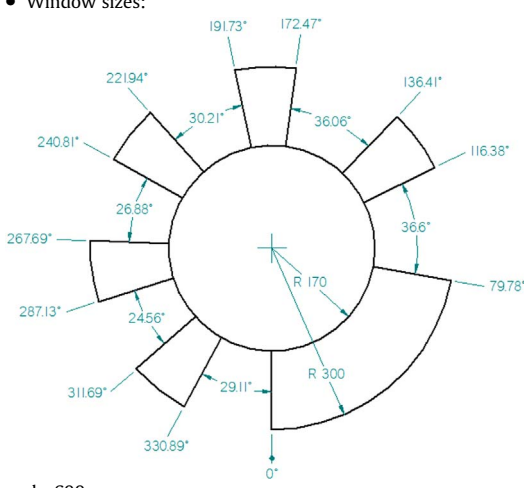
Component	Distance to cold source [m]	Distance to source chopper [m]	Description
13 Band Chopper Disc 1	31.7	10	<ul style="list-style-type: none"> <li>Window size: 140° (contrary to the specified value of 150° used in Ref. [11])</li> </ul>  <ul style="list-style-type: none"> <li>Diameter: 700 mm</li> <li>Normal speed: 14 Hz</li> <li>Selectable Speeds: 7 Hz, 8.4 Hz, 10.5 Hz, 14 Hz, 21 Hz, 42 Hz</li> </ul>
14 Band Chopper Disc 2	31.7	10	<ul style="list-style-type: none"> <li>Window size: 202°</li> </ul>  <ul style="list-style-type: none"> <li>Diameter: 700 mm</li> <li>Normal speed: 14 Hz</li> <li>Selectable Speeds: 7 Hz, 8.4 Hz, 10.5 Hz, 14 Hz, 21 Hz, 42 Hz</li> </ul>
15 Guide	–	–	L=5.75 m, m=3, curved (r=2300 m), H=12.5 cm, W=6 cm
16 Frame Overlap Chopper 2	37.6	15.9	<ul style="list-style-type: none"> <li>Window sizes:</li> </ul>  <ul style="list-style-type: none"> <li>d=600 mm</li> <li>Normal speed: 28 Hz</li> <li>Rotation (viewing from cold source): CW</li> </ul>

Table A1 (continued)

Component	Distance to cold source [m]	Distance to source chopper [m]	Description
17 Slit			<ul style="list-style-type: none"> <li>Selectable Speeds: 14 Hz, 28 Hz, 42 Hz, 56 Hz, 70 Hz</li> </ul> Fixed slit to prevent frame overlap H=10 cm, W=2 cm
18 Guide	–	–	L=3.5 m, m=3, curved (r=2300 m), H=12.5 cm, W=6 cm
19 Guide	–	–	L=5 m, m=3, straight, H=12.5 cm, W=6 cm
20 Polarizing S-bender End of concrete shielding	46.5 47	24.8 25.3	Can be translated in and out of the beam remotely. Guide field reaches outside of the shielding –
21 Measurement position	47–54 (60)	25.3–30 (38)	Optical benches allow setups in direct beam and/or towards the side

## References

- [1] FRM2, Available: (<http://www.frm2.tum.de/en/the-neutron-source/>).
- [2] HFIR, Available: (<https://neutrons.ornl.gov/hfir>).
- [3] ILL, Available: (<https://www.ill.eu/reactor-environment-safety/high-flux-reactor/>).
- [4] SNS, Available: (<http://neutrons.ornl.gov/sns>).
- [5] M. Arai, F. Maekawa, Japan spallation neutron source (JSNS) of J-PARC, Nucl. Phys. News 19 (2009) 34–39.
- [6] LANSCE, Available: (<http://lansce.lanl.gov/>).
- [7] ISIS, Available: (<http://www.isis.stfc.ac.uk/>).
- [8] H. Schober, E. Farhi, F. Mezei, P. Allenspach, K. Andersen, P.M. Bentley, et al., Tailored instrumentation for long-pulse neutron spallation sources, Nucl. Instrum. Methods Phys. Res., Sect. A: Accel., Spectrom., Detect. Assoc. Equip. 589 (2008) 34–46.
- [9] ESS, Realizing DREAM, a Versatile Powder Diffractometer, 2014, 19 Feb 2016. Available: (<https://europeanspallationsource.se/realizing-dream-versatile-powder-diffractometer>).
- [10] F. Mezei, Instrumentation concepts: Advances by innovation and building on experience, The ESS Project, New Science and Technology for the 21st Century, vol. VOL. II, 2002.
- [11] M. Strobl, M. Bulat, K. Habicht, The wavelength frame multiplication chopper system for the ESS test beamline at the BER II reactor – a concept study of a fundamental ESS instrument principle, Nucl. Instrum. Methods Phys. Res. Sect. A: Accel., Spectro., Detect. Assoc. Equip. 705 (2013) 74–84.
- [12] D. Nekrassov, C. Zandler, K. Lieutenant, Design of a wavelength frame multiplication system using acceptance diagrams, Nucl. Instrum. Methods Phys. Res. Sect. A: Accel., Spectrom., Detect. Assoc. Equip. 716 (2013) 71–77.
- [13] E. Laface, M. Rescic, The ESS control box, in: Proceedings of IPAC2012, 2012.
- [14] H.A. Graf, D. Clemens, O. Prok-hnenko, H.J. Bleif, C. Pappas, S. Welzel, et al., Upgrade program for the cold neutron instrumentation of the Helmholtz-Zentrum Berlin, Neutron News 20 (2009) 16.
- [15] T. Krist, A. Tennant, Guide and instrument upgrade at Helmholtz-Zentrum Berlin, Neutron News 25 (2014) 4–7.
- [16] U. Keiderling, A. Wiedenmann, New SANS instrument at the BER II reactor in Berlin, Germany, Physica B: Phys. Condens. Matter 213–214 (1995) 895–897.
- [17] ProxiVision, Available: (<http://www.proxivision.de/products/neutron-detector.html>).
- [18] C. Grünzweig, G. Frei, E. Lehmann, G. Kühne, C. David, Highly absorbing gadolinium test device to characterize the performance of neutron imaging detector systems, Rev. Sci. Instrum. 78 (2007) 053708.
- [19] D. Day, R. Sinclair, Neutron moderator assemblies for pulsed thermal neutron time-of-flight experiments, Nucl. Instrum. Methods 72 (1969) 237–253.
- [20] S. Ikeda, J.M. Carpenter, Wide-energy-range, high-resolution measurements of neutron pulse shapes of polyethylene moderators, Nucl. Instrum. Methods Phys. Res. Sect. A: Accel., Spectrom., Detect. Assoc. Equip. 239 (1985) 536–544.
- [21] K. Lieutenant, Virtual Instrumentation Tool for Neutron Scattering at Pulsed and Continuous Sources. Available: ([http://www.helmholtz-berlin.de/for-schung/oe/em/transport-phenomena/vitess/index\\_en.html](http://www.helmholtz-berlin.de/for-schung/oe/em/transport-phenomena/vitess/index_en.html)).
- [22] F. Mezei, M. Russina, Advances in neutron scattering instrumentation, Proc. SPIE 4785 (2002).
- [23] K. Lieutenant, F. Mezei, J. Neutron Res. 14 (2006).
- [24] M. Russina, G. Káli, Z. Sánta, F. Mezei, First experimental implementation of pulse shaping for neutron diffraction on pulsed sources, Nucl. Instrum. Methods Phys. Res., Sect. A: Accel., Spectrom., Detect. Assoc. Equip. 654 (2011) 383–389.
- [25] H.G. Priesmeyer, M. Stalder, S. Vogel, K. Meggers, R. Bless, W. Trela, Bragg-edge transmission as an additional tool for strain measurements, Textures Microstruct. 33 (1999) 173–185.
- [26] R. Woracek, D. Penumadu, N. Kardjilov, A. Hilger, M. Boin, J. Banhart, et al., 3D mapping of crystallographic phase distribution using energy-selective neutron tomography, Adv. Mater. (2014), pp. n/a–n/a.
- [27] M. Strobl, R. Woracek, N. Kardjilov, A. Hilger, R. Wimpory, A. Tremsin, et al., Time-of-flight neutron imaging for spatially resolved strain investigations based on Bragg edge transmission at a reactor source, Nucl. Instrum. Methods Phys. Res. Sect. A: Accel., Spectrom., Detect. Assoc. Equip. 680 (2012) 27–34.
- [28] N. Kardjilov, A. Hilger, I. Manke, R. Woracek, J. Banhart, CONRAD-2: the new neutron imaging instrument at the Helmholtz-Zentrum Berlin, J. Appl. Crystallogr. 49 (2016).
- [29] The Network Integrated Control System (NICOS), Available: (<http://cdn.frm2.tum.de/fileadmin/stuff/services/ITServices/nicos-2.0/dirhtml/>).
- [30] 2016 EPICS Collaboration Meeting. Available: (<https://indico.esss.lu.se/event/507/overview>).
- [31] Z. Salhi, E. Babcock, R. Gainov, K. Bussmann, H. Kaemmerling, P. Pistel, et al., First result from the magic-PASTIS using large 3He SEOP-polarized GE180 doughnut cell, J. Phys.: Confer. Ser. (2016) 012013.
- [32] W.G. Bouwman, C.P. Duif, R. Gähler, Spatial modulation of a neutron beam by Larmor precession, Physica B-Condens. Matter 404 (2009) 2585–2589.
- [33] M. Strobl, M. Sales, J. Plomp, W.G. Bouwman, A.S. Tremsin, A. Kaestner, et al., Quantitative neutron dark-field imaging through spin-echo interferometry, Sci. Rep. 5 (2015) 16576.
- [34] M. Strobl, A. Tremsin, A. Hilger, F. Wieder, N. Kardjilov, I. Manke, et al., TOF-SEMSANS – time-of-flight spin-echo modulated small-angle neutron scattering, J. Appl. Phys. 112 (2012) 014503.
- [35] B. Betz, R. Harti, M. Strobl, J. Hovind, A. Kaestner, E. Lehmann, et al., Quantification of the sensitivity range in neutron dark-field imaging, Rev. Sci. Instrum. 86 (2015) 123704.
- [36] M. Strobl, General solution for quantitative dark-field contrast imaging with grating interferometers, Sci. Rep. 4 (2014) 7243, 11/28/online 2014.
- [37] M. Strobl, B. Betz, R. Harti, A. Hilger, N. Kardjilov, I. Manke, et al., Wavelength-dispersive dark-field contrast: micrometre structure resolution in neutron imaging with gratings, J. Appl. Crystallogr. 49 (2016).
- [38] R. Woracek, D. Penumadu, N. Kardjilov, A. Hilger, M. Strobl, R.C. Wimpory, et al., Neutron Bragg-edge-imaging for strain mapping under in situ tensile loading, J. Appl. Phys. 109 (2011) 093506.
- [39] J.R. Santisteban, L. Edwards, A. Steuwer, P.J. Withers, Time-of-flight neutron transmission diffraction, J. Appl. Crystallogr. 34 (2001) 289–297.
- [40] R. Woracek, J. Bunn, D. Penumadu, A. Tremsin, A. Siriruk, N. Kardjilov, et al., Methodology for combined neutron diffraction and Bragg edge imaging, in: MRS Proceedings, 2013, pp. mrsf12-1528-vv08-04.